# DEVELOPMENT OF A SIMULTANEOUS MULTI-SLICE RADIOFREQUENCY PULSE IN A SEQUENCE PROGRAMMING ENVIRONMENT WITH IMPLEMENTATION IN AN ILL-CONDITIONED CONTROLLED ALIASING RECONSTRUCTION SIMULATION

Christian Pecora

A thesis submitted to the faculty at the University of North Carolina at Chapel Hill in partial fulfillment of the requirements for the degree of Master of Science in the Department of Biomedical Engineering in the School of Medicine.

Chapel Hill
2016

Approved by:

Hongyu An

David Lalush

Shumin Wang

ABSTRACT

Christian Pecora: Development of a Simultaneous Multi-Slice Radiofrequency Pulse in a Sequence Programming Environment with Implementation in an Ill-Conditioned Controlled Aliasing Reconstruction Simulation
(Under the direction of Hongyu An)

Scan time acceleration, with many clinical and research applications, has been an active research area in magnetic resonance imaging with the introduction of new pulse sequences, parallel imaging (PI) techniques, and methods to acquire multiple slices simultaneously. The development of novel uses for the latest techniques is facilitated by the ability to create customized in-house pulse sequences. In this work, a simultaneous multi-slice radiofrequency (RF) pulse was developed within a sequence programming environment. This RF pulse was then utilized in a reconstruction simulation of a controlled aliasing in parallel imaging results in higher acceleration (CAIPIRINHA) acquisition with an ill-conditioned coil geometry. The slice-excitation behavior of the in-house developed RF pulse was affirmed along with a successful confirmation of the image reconstruction benefits of the CAIPIRINHA technique. This provided a demonstration of sequence development and the ability to implement CAIPIRINHA in future PI studies requiring a demanding coil-array geometry.

To my son Angelo Valentino Pecora, whose strength and bravery has been my inspiration.

ACKNOWLEDGEMENTS

I would like to thank my committee member and advisor Dr. Hongyu An for her extensive knowledge and guidance throughout this project. The amount of patience and consideration she provided me during the development of my skills facilitated the growth of the confidence I needed to push personal boundaries and achieve my goals. I also would like to thank my committee member Dr. David S. Lalush for his continued guidance and input on all my signal processing and reconstruction questions. Furthermore, I want to express thanks to my committee member Dr. Shumin Wang for providing his insight during my project. In addition, I want to thank my good friend Dr. Cihat Eldeniz for helping me acquire some of the image data used during the project, providing guidance on the MRI scanner, and coaching me through many aspects of pulse sequence development. Moreover, I would like to thank my wife Dr. Keri A. Pecora for not only her continued love and support but also for acting as a mathematical encyclopedia with no boundaries, answering the countless questions I had during the course of my research. Lastly, I would like to thank the University of North Carolina at Chapel Hill Biomedical Research Imaging Center (BRIC) and North Carolina State University for the ability to use the imaging hardware and other campus resources in addition to providing a wonderful culture of learning that fostered my growth as a scholar.

TABLE OF CONTENTS

LIST OF FIGURES

# LIST OF ABBREVIATIONS

| | |
|---|---|
| ACR | The American College of Radiology |
| ADC | Analog-to-digital converter |
| CAIPIRINHA | Controlled aliasing in parallel imaging results in higher acceleration |
| CFT | Continuous Fourier transform |
| COZA | Combined zeugmatography and array |
| DFT | Discrete Fourier transform |
| EPI | Echo planar imaging |
| FFT | Fast Fourier transform |
| FLASH | Fast low angle shot |
| FOV | Field of view |
| GRAPPA | Generalized autocalibrating partially parallel acquisitions |
| GRE | Gradient recalled echo |
| ICFT | Inverse continuous Fourier transform |
| IDFT | Inverse discrete Fourier transform |
| IFFT | Inverse fast Fourier transform |
| MRI | Magnetic resonance imaging |
| PI | Parallel imaging |
| POMP | Phase-offset multiplanar |
| RF | Radiofrequency |
| SDE | Sequence development environment |
| SENSE | Sensitivity encoding |
| SMA | Simultaneous multi-slice acquisition |

| | |
|---|---|
| SMASH | Simultaneous acquisition of spatial harmonics |
| SNR | Signal-to-noise ratio |
| SOS | Sum of squares |
| TSE | Turbo spin echo |
| UI | User interface |

LIST OF SYMBOLS

| | |
|---|---|
| $B_0$ | Static magnetic field magnitude |
| $\vec{B}_0$ | Static magnetic field |
| $\vec{B}_1(t)$ | Time-varying magnetic field of RF pulse |
| $\vec{B}_{net}$ | Net time-varying and static magnetic fields applied |
| $c_\beta$ | Sensitivity of coil $\beta$ |
| $C$ | Coil sensitivity matrix |
| $C_{\beta,p}$ | Elements of $C$ for the $\beta^{th}$ coil at pixel $p$ |
| $\Delta E$ | Energy difference between the up and down spin states |
| $\mathcal{F}$ | Fourier transform operator |
| $F(x)$ | CFT input for real-valued $x$ |
| $f(\xi)$ | CFT coefficient for continuous real-valued frequency $\xi$ |
| $F_n$ | DFT input for data sample $n$ |
| $FOV_{object}$ | The size of the imaged object in the phase-encoding direction |
| $f_\upsilon$ | DFT coefficient for discrete frequency sample υ |
| $f_{os}$ | Offset frequency |
| $g^p_{CAIPI}$ | CAIPIRINHA g-factor at pixel $p$ |
| $g^p_{SENSE}$ | SENSE g-factor at pixel $p$ |
| $G_x$ | Magnetic field gradient along the $x$ direction |
| $G_y$ | Magnetic field gradient along the $y$ direction |
| $G_z$ | Magnetic field gradient along the $z$ direction |
| $\Delta G$ | Gradient amplitude increment |

| | |
|---|---|
| $\Delta G_y$ | Gradient amplitude increment along the $y$ direction |
| $i_\beta$ | Image matrix of pixel intensities for coil $\beta$ |
| $\vec{I}_p$ | Pixel intensity vector for pixel $p$ from each $i_\beta$ |
| $k_x$ | Spatial frequency along the $x$ direction |
| $k_y$ | Spatial frequency along the $y$ direction |
| $\Delta k_y$ | Phase-encoding line increment |
| $\Delta k$ | $k$-space position increment |
| $l$ | Slice number |
| $M_0$ | Initial magnitude of magnetization oriented along $\vec{B}_0$ |
| $M_z$ | Magnitude of magnetization along the $z$ direction |
| $\vec{M}$ | Net magnetization vector |
| $\vec{M}_\parallel$ | Component vector of $\vec{M}$ along the $z$ direction |
| $\vec{M}_\perp$ | Component vector of $\vec{M}$ in the transverse plane |
| $n_{pe}$ | Phase-encoding step |
| $N_s$ | Number of samples in the data set |
| $N_d$ | Dimensions of image matrix |
| $NS$ | Number of simultaneous slices |
| $p$ | Image pixel number |
| $R$ | $k$-space subencoding acceleration factor |
| $N_c$ | Number of coils |
| $\vec{r}_p$ | Vector position of pixel $p$ |
| $s$ | Spin number |

| | |
|---|---|
| $S$ | Signal intensity measured by coil |
| $\vec{S}$ | Spin angular momentum vector |
| $SNR_{CAIPI}^{p}$ | CAIPIRINHA SNR at pixel $p$ |
| $SNR_{SENSE}^{p}$ | SENSE SNR at pixel $p$ |
| $SNR_{UA}^{p}$ | SNR for pixel $p$ from an unaccelerated acquisition |
| $T$ | Temperature in Kelvins |
| $\vec{T}$ | Torque vector |
| $T_1$ | Spin-lattice relaxation time constant |
| $T_2$ | Spin-spin relaxation time constant |
| $T_E$ | Echo time |
| $T_R$ | Repetition time |
| $U$ | SENSE unfolding matrix |
| $\Delta y(l)$ | Spatial shift in the phase-encoding direction for slice $l$ |
| $\Delta y$ | Spatial shift in the phase-encoding direction |
| $\Delta z$ | Distance offset from the scanner isocenter in the $z$ direction |
| $\beta$ | Coil number |
| $\gamma_p$ | Gyromagnetic ratio for a proton |
| $\theta$ | RF flip angle |
| $\vec{\mu}_p$ | Magnetic moment vector for a proton |
| $\xi$ | Continuous frequency |
| $\rho$ | Proton spin density |
| $\tau_{pe}$ | Phase-encoding gradient duration |

| | |
|---|---|
| $\phi$ | Phase of $\vec{M}_{\perp}$ |
| $\phi_m$ | CAIPIRINHA phase alteration for step $m$ |
| $\psi$ | Coil-array noise correlation matrix |
| $\omega_L$ | Larmor frequency |
| $\vec{\chi}$ | Vector of reconstructed pixel intensities in SENSE |
| $\|\uparrow\rangle$ | Up spin state |
| $\|\downarrow\rangle$ | Down spin state |

# CHAPTER 1: INTRODUCTION

Since its first use in the clinical setting, magnetic resonance imaging (MRI) has provided an unprecedented, non-invasive view of internal anatomy. What is particularly remarkable is its ability to provide detailed, soft-tissue contrast in a multitude of ways depending on the imaging protocol utilized. Over the years, MRI has been the subject of many modifications to increase hardware capabilities and develop new pulse sequences and techniques to increase patient comfort, decrease scan time, and further advanced research and clinical applications.

Patient comfort can be affected in many ways including patient-related factors like phobias and health conditions that affect the ability to pause breathing and remain still during some studies. In addition, scanner-related factors including radiofrequency (RF) pulse heating, peripheral nerve stimulation, and loud gradient sounds arising from movement of the coils during a protocol can impact a patient's experience.

Acquisition time plays a large role in patient comfort and image quality. The time spent in the scanner will require the patient to endure more scanner-related effects in addition to maintaining uncomfortable positions potentially aggravated by health conditions. Moreover, many dynamic studies utilizing diffusion imaging and functional MRI require high quality images taken at a very high temporal resolution to avoid image quality issues like motion artifacts.

Therefore, many efforts have focused on decreasing acquisition time while maintaining image quality. Imaging with multiple coil detectors to acquire data in parallel using the spatial

sensitivity of the coils and simultaneous multi-slice acquisition (SMA) are two particular directions that have been pursued since the 1980s to achieve a reduced scan time.

Modern parallel imaging (PI) techniques fall into two general categories depending on whether the parallel data is calculated in $k$-space or in the spatial domain. An example of a popular $k$-space method is generalized autocalibrating partially parallel acquisitions (GRAPPA) [1], which reconstructs missing spatial frequencies while spatial-domain techniques including sensitivity encoding (SENSE) [2] perform a separation of aliased pixels. In addition, SMA techniques [3-5] that utilize PI methods to assist with reconstruction have been developed allowing for higher potential scan time reductions.

Spatial-domain methods can suffer signal-to-noise ratio (SNR) penalties due to the challenging coil-array geometry imposed on the matrix-based inversion reconstruction which can limit their application in scenarios using demanding geometries [4]. Controlled aliasing in parallel imaging results in higher acceleration (CAIPIRINHA) is a spatial-domain based PI method developed in [4] that can improve the condition of the reconstruction problem by applying spatial shifts to the slices in a SMA, increasing the spatial sensitivity differences that the slice reconstruction relies on.

Many of these methods can be incorporated into existing sequences, extending their application to novel problems. Therefore, it is beneficial to have the ability to build new in-house sequences that can incorporate the latest advancements into upcoming research. This customization can be done using the MRI manufacturer's sequence development environment.

In this work, an implementation and evaluation of the CAIPIRINHA technique will be performed with two specific aims:

## Specific aim 1

Develop an in-house simultaneous two-slice excitation RF pulse with CAIPIRINHA phase cycling within the Siemens sequence development environment (SDE), incorporate the pulse into a fast low angle shot (FLASH) sequence, and confirm the accuracy of the slice excitation locations.

## Specific aim 2

Use the FLASH sequence with the SMA RF pulse developed in specific aim 1 to acquire images of a phantom and simulate the benefits of the CAIPIRINHA reconstruction technique when used in an application with an ill-conditioned matrix reconstruction due to a demanding coil-array geometry.

## CHAPTER 2: MRI PHYSICS AND IMAGE FORMATION

### 2.1: Origin of the MRI signal

The signals producing the raw data for MRI images ultimately derive from the behavior of the magnetic moment of a proton in response to applied magnetic fields. The magnetic moment arises from an intrinsic quantum property $\vec{S}$ called spin angular momentum or spin. Elementary particles like electrons and hadrons like the proton possess this property and by extension many atomic nuclei. The amount of spin that a particle possesses depends on its spin quantum number $s$; fermions have half-integer values and bosons have integer values. The magnitude of spin is quantized by $s$ according to the solution of the Schrodinger partial differential equation and given in terms of the reduced Planck's constant $\hbar$ by

$$\left\|\vec{S}\right\| = \sqrt{s(s+1)}\hbar. \quad s = 0, \frac{1}{2}, 1, \frac{3}{2} \ldots, \tag{1}$$

For a proton, $s = 1/2$. When measured along a particular axis in the Cartesian coordinate plane, it has been experimentally shown that the proton can be found in two spin states: up $|\uparrow\rangle$ and down $|\downarrow\rangle$ which are parallel and antiparallel along the measured direction respectively. The component of the spin vector along the measured axis is $(1/2)\hbar$ for the $|\uparrow\rangle$ state and $(-1/2)\hbar$ for the $|\downarrow\rangle$ state.

Although there is no classical intuition for this property, an analogy can be made to an object rotating about its own axis. This intrinsic angular momentum together with the positive charge of the proton can be loosely visualized as a rotating positive charge giving

rise to a magnetic moment $\vec{\mu}_p$which can be given in terms of the spin vector $\vec{S}$ and a constant called the gyromagnetic ratio $\gamma_p$ by

$$\vec{\mu}_p = \gamma_p \vec{S}. \tag{2}$$

These spin vectors will be oriented at a quantized angle relative to the main axis of measurement. The sharp component of the spin vector corresponds to the main axis and the fuzzy components of the spin vector correspond to the other two axes. Therefore, there exists a probability that the spin vector will be at any location within a cone oriented upward or downward corresponding to the $|\uparrow\rangle$ or $|\downarrow\rangle$ state respectively, as illustrated in Figure 2.1.

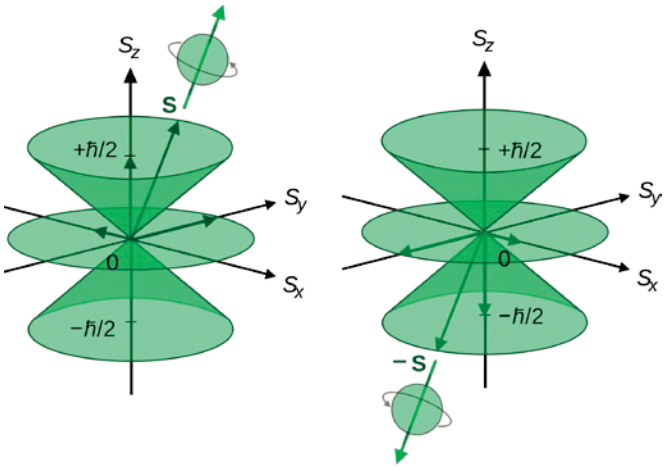


Figure 2.1: Possible positions for a spin vector measured along the $z$ direction [6].

In a sample of protons uninfluenced by electromagnetic fields, their spin vectors will be oriented randomly. However, if a magnetic field is applied to the sample along a particular direction, the expected value for each spin will precess around direction of the applied magnetic field within one of the cones in Figure 2.1. With the applied magnetic field, an energy difference develops between the two states resulting in a slightly larger proportion of spins being found in the lower energy $|\uparrow\rangle$ state. This energy difference for a static field $\vec{B}_0$ with magnitude $B_0$ is given by

$$\Delta E = \gamma_p \hbar B_0. \tag{3}$$

The proportion of spins in the $|\uparrow\rangle$ and $|\downarrow\rangle$ state depends not only on the magnetic field strength but also on temperature. This relationship is governed by the Boltzmann distribution,

$$\frac{\text{number of } |\uparrow\rangle}{\text{number of } |\downarrow\rangle} = e^{\frac{\Delta E}{k_B T}} \tag{4}$$

which gives the ratio of spins in the $|\uparrow\rangle$ and $|\downarrow\rangle$ states, where $k_B$ is Boltzmann's constant and $T$ is temperature in Kelvins.

Under the influence of a magnetic field, the spin vectors will each have a random precessional phase resulting in a net cancellation such that the expected value of the vector sum of each $\vec{\mu}_p$ in the sample will produce a net magnetization vector $\vec{M}$ that is oriented along the direction of the applied magnetic field, which in this case is along the $z$-axis as shown in Figure 2.2.

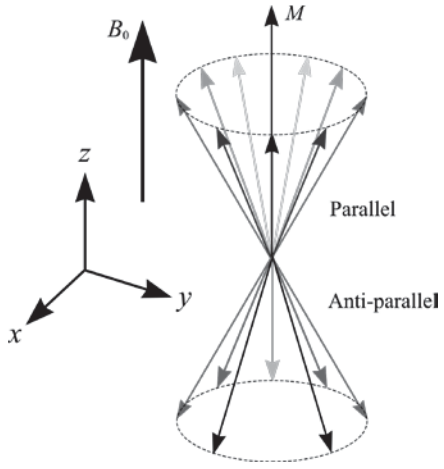


Figure 2.2: The net magnetization vector $\vec{M}$ formed from the vector sum of many $\vec{\mu}_p$ [7].

The magnitude of $\vec{M}$ affects the strength of the signal that can be generated during a scan and is directly dependent on the proportion of spins that are in the $|\uparrow\rangle$ state.

The individual spins which comprise $\vec{M}$ are assumed to experience the same applied magnetic field. The spins meeting this condition are known as a spin isochromat. Many isochromats can exist within a given small region corresponding to spatially-varying magnetic fields that may be felt.

The ensemble behavior of the spins which comprise $\vec{M}$ has been shown to be classical so its quantum origin can be ignored for most applications.

## 2.2: Bloch equations of motion

When $\vec{M}$ is placed in a magnetic field, it will experience a magnetic torque $\vec{T}$ produced by the interaction between itself and the applied magnetic field given by,

$$\vec{T} = \vec{M} \times \vec{B}_{net} \tag{5}$$

where $\vec{B}_{net}$ represents the net static and time-varying fields applied. This torque is analogous to the torque experienced by a spinning top under the influence of the gravitational field. This torque will cause the tip of $\vec{M}$ to precess around the direction of the applied magnetic field. This behavior can be modeled by the vector differential equation

$$\frac{d\vec{M}}{dt} = \gamma_p \vec{M} \times \vec{B}_{net}. \tag{6}$$

The resulting precessional frequency, which can be derived by analyzing the form of (6) and the associated geometry in the coordinate plane, is known as the Larmor frequency which is given by,

$$\omega_L = \gamma_p B_{net} \tag{7}$$

where $B_{net}$ is the magnitude of the applied magnetic field. The Larmor frequency will allow the analysis of the behavior of $\vec{M}$ from its phase, suggesting a method for the acquisition of raw data to be discussed in section 2.4.

While providing a simple way to visualize the precessing spins, the differential equation (6) does not include relaxation effects which are caused by the interactions between the spins that compose $\vec{M}$ and their surroundings. An imaging experiment begins with the manipulation of some quantity of $\vec{M}$ into the transverse plane where it can be measured. However, many important image parameters rely on when measurements are taken, providing a view of $\vec{M}$ at a given time point. The most notable of these effects are associated with the exponential time constants $T_1$ and $T_2$.

To simplify the analysis of the time evolution of $\vec{M}$, it can written it terms of the component $\vec{M}_{\parallel} = M_z\hat{z}$ in the direction of the static magnetic field $\vec{B}_0 = B_0\hat{z}$ and the components in the transverse plane, $\vec{M}_{\perp} = M_x\hat{x} + M_y\hat{y}$.

Spin-lattice relaxation or $T_1$ represents the decay of the transverse magnetization back to fully longitudinal magnetization and this occurs because of the exchange of energy between the spins that are precessing in the transverse plane with the surrounding chemical species. This relaxation process is illustrated in Figure 2.3. This transfer of energy results in $\vec{M}_{\perp}$ aligning itself back with the static magnetic field. This process is given by an exponential increase in the longitudinal magnetization with the $T_1$ value representing when $\vec{M}_{\parallel}$ has recovered to approximately 63% of its initial value.

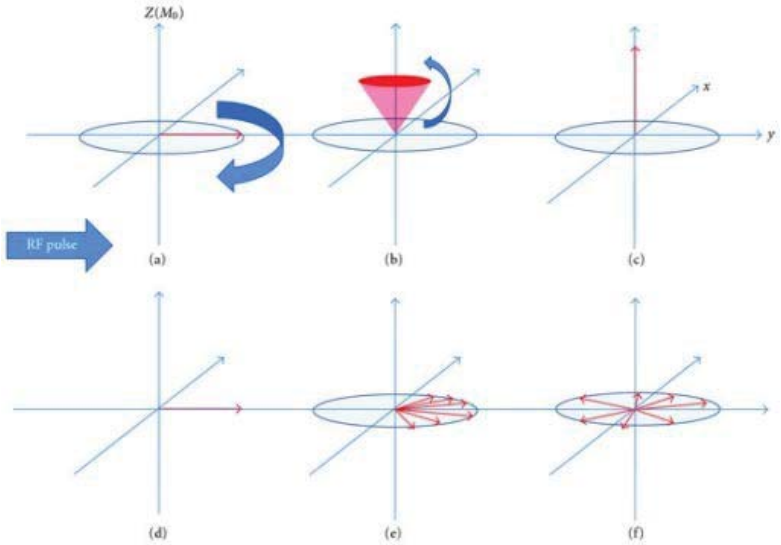

Figure 2.3: $T_1$ and $T_2$ relaxation proceeding in (a-c) and (d-f) respectively [8].

Spin-spin relaxation or $T_2$ occurs because of an interaction between neighboring protons causing each other to see a slightly different local magnetic field, resulting in an altered Larmor frequency and dephasing of the spins in the transverse plane. This causes the components of $\vec{M}_\perp$ to point in various directions giving vector cancellation and decreased signal. The process of $T_2$ relaxation, illustrated in Figure 2.3, represents only an exchange in energy between spins rather than a decrease in energy from the system that is seen in $T_1$. This behavior is given by an exponential decrease, with $T_2$ representing the time it takes for the transverse magnetization to decrease to 37% of its initial value.

The chemical environments of various tissues relax the resident spins in different ways, providing for tissue-dependent $T_1$ and $T_2$ constants. These tissue constants and the measurement timings of a particular protocol are directly involved with the strength of the signal that can be measured, giving MRI the ability to provide contrast to different tissues in an image. The effects of $T_1$ and $T_2$ relaxation can be incorporated into (6) giving

$$\frac{d\vec{M}}{dt} = \gamma_p \vec{M} \times \vec{B}_{net} + \frac{1}{T_1}(M_0 - M_z)\hat{z} - \frac{1}{T_2}\vec{M}_{\perp}. \quad (8)$$

With these additions, it becomes possible to more accurately model the behavior of $\vec{M}$.

## 2.3: Mathematical framework for image formation

The dominant mathematical foundation in MRI that underpins the acquisition of raw data and the reconstruction of an image is the Fourier transform.

The continuous Fourier transform (CFT) is an integral transform that in general takes as an input a complex-valued function and produces a complex-valued function of frequency $\xi$ given here in one dimension as

$$f(\xi) = \int_{-\infty}^{\infty} F(x) e^{-j2\pi\xi x}\, dx. \quad (9)$$

Common mathematical function spaces on which the Fourier transform operates are those with an inner-product structure. In these spaces, there is a generalized concept of an orthonormal basis from linear algebra onto which the functions in that space can be projected and then expressed as a weighted linear combination of the basis components.

The Fourier transform will in general produce for each real-valued frequency $\xi$ a complex value called the Fourier coefficient that represents the contribution a particular complex sinusoidal frequency in that basis makes to form the input function. A full listing of the Fourier coefficients for the corresponding frequencies is known as the input functions' frequency spectrum. By projecting an input function onto each component of the frequency basis, an alternative view of the function is produced giving a unique insight into its periodic behavior. The intimately related inverse continuous Fourier transform (ICFT) that allows the reconstruction of the original data points based on the CFT spectral data is given by

$$F(x) = \int_{-\infty}^{\infty} f(\xi) e^{j2\pi\xi x}\, d\xi. \tag{10}$$

Although theoretically valid, the continuous Fourier transform is not useful when dealing with a finite set of uniformly sampled data seen in modern digital systems and in MRI image reconstruction. In this case, a more applicable form of the Fourier transform is known as the discrete Fourier transform (DFT) given by

$$f_v = \frac{1}{N_s} \sum_{n=0}^{N_s-1} F_n e^{-j2\pi \frac{v}{N_s} n}. \tag{11}$$

This form takes as input a finite set of discrete, complex data points $F_n$ and outputs a complex value $f_v$ quantifying the contribution each complex sinusoid, with discrete frequency index $v$, makes to form the input function.

The inverse discrete Fourier transform (IDFT) allows the reconstruction of the original data points based on the DFT spectral data and is given by

$$F_n = \sum_{v=0}^{N_s-1} f_v e^{j2\pi \frac{v}{N_s} n}. \tag{12}$$

An efficient implementation of the DFT and IFT that is used to operate on digital data in modern applications including the reconstruction of MRI images is known as the fast Fourier transform (FFT) and its inverse (IFFT) developed in [9].

In standard Fourier-based MRI acquisitions, the raw data produced are the Fourier transform coefficients for all the spatial frequencies sampled. After processing, the raw data is input into the 2D IFFT (for a 2D slice) or 3D IFFT (for a 3D volume acquisition) producing the image. The quality of the resulting image is dependent the data input to the IFFT; if the raw data is distorted, features not found in the object may be present in the image potentially masking

pathologies. Producing an artifact-free image is influenced by many factors including the protocol used, movement and tissue characteristics of the objects imaged, environmental disturbances, and scanner hardware.

## 2.4: Collection of raw data for a two-dimensional image

To form an image, the spins composing $\vec{M}$ at different locations in the imaged object must be perturbed from their equilibrium under the influence of a static magnetic field $B_0\hat{z}$. The activation of the spins using additional magnetic fields in the form of spatial gradients and RF pulses will allow them to produce a signal that is spatial localized and sampled, forming the raw data that a two-dimensional image will be reconstructed from.

### 2.4.1: RF pulse excitation of $\vec{M}$

Signal generation begins with the transfer of some of the longitudinal magnetization $\vec{M}_{\parallel}$ to the transverse plane where it can induce a voltage in a receiver coil by Faraday's law of induction. This behavior becomes easier to analyze if it is viewed in a reference frame that rotates at the Larmor frequency. If this is done, $\vec{M}$ appears stationary and an analysis of effects other than the static magnetic field can be performed.

Resonance in MRI is a crucial effect during the signal-generating step when $\vec{M}$ responds to a time-varying magnetic field $\vec{B}_1(t)$. This magnetic field, in the form of a RF pulse that perturbs $\vec{M}$ from its alignment with the static magnetic field, causes $\vec{M}_{\perp}$ to form in the transverse plane.

The resonance condition is achieved if the frequency of the applied magnetic field is the same as the Larmor frequency of the spins that compose $\vec{M}$ at a given location. If this condition is met, energy will be most efficiently deposited into the system and cause the magnetization to rotate about an axis depending on the direction along which the RF pulse is applied.

For example, if a RF pulse is applied along the positive $x$-axis, a torque will be generated which will cause $\vec{M}$ to swing toward the transverse plane with an axis of rotation along the $x$-axis. When viewed in the rotating reference frame, the magnetization will appear stationary and form an angle with the $z$-axis as shown in Figure 2.4. The angle $\theta$, called the flip angle, is an important parameter influencing the image quality obtained from an acquisition and is a characteristic of the RF pulse. The phase of the applied RF pulse will determine the initial phase $\phi$ of $\vec{M}_{\perp}$ in the transverse plane.

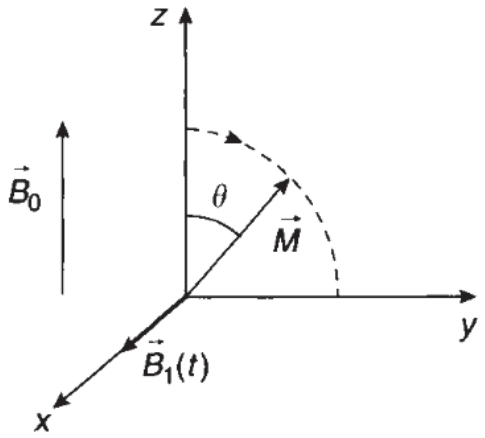


Figure 2.4: Excitation of $\vec{M}$ with an applied RF pulse $\vec{B}_1(t)$, with subsequent formation of $\vec{M}_{\perp}$ in the transverse plane [10, p. 68].

### 2.4.2: Slice selection

The ability to image only a certain section of a volume requires that the signal come from only the desired section. This selectivity depends on the precise manipulations of the spins in different regions of the body to be on resonance with the RF pulse that will be applied to excite the spins. Restricting the volume that meets the resonance condition is made possible by the use of magnetic field gradients.

Magnetic field gradients are magnetic fields that have spatially-varying amplitude. With the applied gradient, spins in each location will feel a different magnetic field as a result of the gradient adding or subtracting from the static magnetic field $\vec{B}_0$ strength that each sees equally. Therefore, the Larmor frequency will be given at each location by,

$$\omega_L = \gamma_p[\vec{B}_0 + G_Z \Delta z] \tag{13}$$

where in this example $G_z$ represents a constant gradient applied along the $z$ direction and $\Delta z$ represents the offset from the isocenter of the magnet where $G_z = 0$. Equation (13) also holds for gradients applied along other directions.

Consider a patient oriented with their head along the positive $z$ direction that forms the long axis of the magnet bore within which a static magnetic field $B_0\hat{z}$ is applied. A transverse slice can be selected by applying a slice-selection gradient in the $z$ direction giving each location a different Larmor frequency as in (13) while concurrently applying a RF pulse whose excitation profile includes only the Larmor frequencies represented in the volume of interest along that direction. An example of transverse slice selection is shown in Figure 2.5.

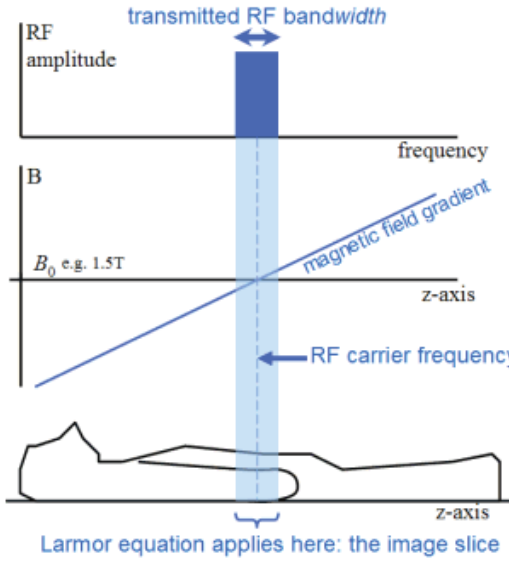


Figure 2.5: Selection of transverse slice along $z$ direction [11].

The magnetization $\vec{M}$ from all locations in the volume selected will now have a component in the transverse plane which induces a voltage in the surrounding receiver coils providing a component of the raw data which is sampled by an analog-to-digital converter (ADC). Figure 2.6 shows a schematic of a quadrature receive coil configuration that measures a complex signal in the transverse plane.

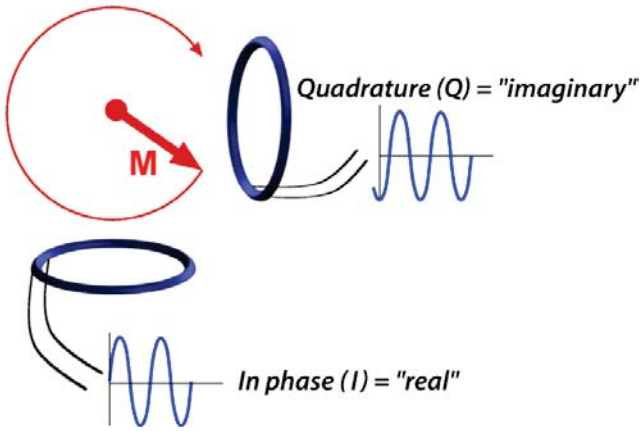


Figure 2.6: Measurement of $\vec{M}_{\perp}$ using a quadrature coil configuration [12].

After slice selection, the transverse magnetization will be precessing at the same frequency after removal of the gradient. Therefore, the composite signal received by the coil from all locations gives no information about where its components arose from within the plane of the slice. Incorporating spatial-encoding gradients along the two directions in the plane of the slice allows for the resolution of information along those directions.

### 2.4.3: Two-dimensional spatial encoding

With the Fourier transform as the basis for data acquisition, it will be seen that the MRI scanner is physically implementing this integral transform through the use of magnetic field gradients and the integration of the signal produced by the perturbed spins.

If the acquisition of a two-dimensional slice is desired, two types of spatial encoding will be used: phase encoding and frequency encoding.

Frequency encoding provides a way to distinguish spins from each other along a given direction in the plane. This is done by applying a gradient of a given magnitude along that direction in the plane while the signal is being sampled by the ADC. The spins will acquire a phase in the transverse plane that depends on its location, the magnitude of the gradient, and the duration the gradient is applied. For example, if frequency encoding is performed along the $x$ direction, the phase that a spin develops will depend on its location given by the relationship

$$\phi(x,t) = -\gamma_p x \int_0^t G_x(t')\, dt'. \tag{14}$$

Equation 14 shows that the applied gradient $G_x$ produces a phase distribution that has the effect of sampling a particular spatial frequency when the receiver coil integrates the signal from all the spins. If signal detection and thermodynamic effects on a group of spins are considered, the measured $\vec{M}_\perp$ can be described by the effective spin density $\rho(x)$ for a simple one-dimensional scenario. If the spin density can be given in terms of a complex exponential, the signal sampled by the coils can be represented as a Fourier transform of the spin density,

$$S(k_x) = \int \rho(x)\, e^{-j2\pi k_x x} dx \tag{15}$$

where $k_x$ is the spatial frequency sampled at time $t$ and is given by

$$k_x(t) = \frac{\gamma_p}{2\pi} \int_0^t G_x(t') dt'. \tag{16}$$

Frequency encoding allows for the distinction of spins along one direction in the plane. However, reconstruction of a two-dimensional slice requires a way to distinguish spins along the other in-plane direction. Frequency encoding cannot be performed in both in-plane directions

because an ambiguity in spin phase would result. Therefore, a separate step called phase encoding is required.

The process of phase encoding differs from frequency encoding in two main ways: phase encoding is not applied while the signal is being sampled by the ADC, and at each application only one spatial frequency is sampled, requiring multiple steps to acquire all the spatial frequencies along this direction. At each step, the gradient amplitude varies while its duration remains constant.

During each phase-encoding step $n_{pe}$, a gradient $G$ is applied along the non-frequency-encoding direction for a step-independent duration $\tau_{pe}$ at an amplitude given by the increment $n_{pe}\Delta G$. For example, with phase encoding performed along the $y$ direction, a distribution of phases is set up by

$$\phi(y, n_{pe}) = -\gamma_p n_{pe} \Delta G_y y \tau_{pe}. \tag{17}$$

However, unlike frequency encoding, the gradient is turned off leaving that distribution of phases constant along this direction. This results in the sampling of one particular spatial frequency while all of the desired spatial frequencies are sampled along the frequency-encoding direction during readout. To sample all the spatial frequencies needed in the phase-encoding direction, the gradient amplitude must be varied at each step. This amplitude increment allows the selection of a different spatial frequency $k_y$, given as a function of the phase-encoding step by

$$k_y(n_{pe}) = \frac{\gamma_p}{2\pi} n_{pe} \Delta G_y \tau_{pe}. \tag{18}$$

The analogy made to the Fourier transform of the spin density in (15) can be made along this direction as well.

The complete signal that is integrated by the receiver coil during a two-dimensional image acquisition when slice selection, frequency encoding, and phase encoding are performed can be represented by the two-dimensional Fourier transform of the spin density as

$$S(k_x, k_y) = \iint \rho(x, y) e^{-j2\pi(k_x x + k_y y)} dx dy. \tag{19}$$

Note that (19) does not take into account signal weighting due to protocol parameters.

The two-dimensional spatial frequencies characterizing the sampled raw data are represented in a coordinate plane called $k$-space. Reconstruction of $k$-space data into an image slice is performed by an IFFT. An example of $k$-space data and the corresponding reconstructed slice are shown in Figure 2.7.

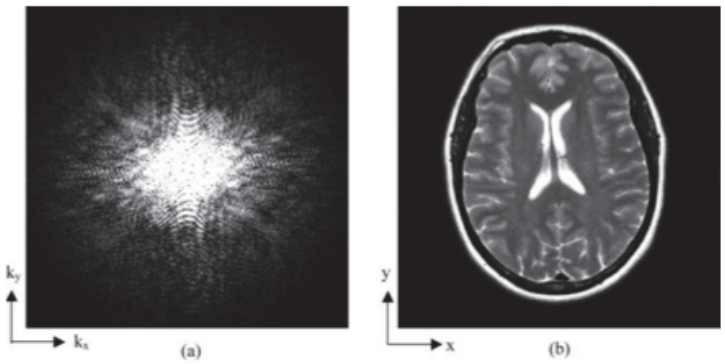


Figure 2.7: $K$-space data (a) and the reconstructed image after IFFT (b) [13, p. 148].

## 2.5: Pulse sequences

The versatility of MRI comes from the many ways the behavior of the spins can be manipulated by a combination of RF pulses and gradient events. The well-defined sequence of perturbing events that are used to produce the desired tissue contrast for a particular application is known collectively as a pulse sequence. It includes slice-selection gradients, spatial-encoding gradients, RF pulses, and data collection events made by the ADC. The effect of these events on image contrast is determined by important timing parameters which include when the signal is

sampled relative to the excitation RF pulse known as the echo time $T_E$ and the time interval between successive excitation RF pulses known as the repetition time $T_R$. A convenient way of viewing these pulse sequence events is through a diagram.

A pulse sequence diagram can have many forms and can include a line devoted to each different type of event that can take place during an imaging protocol. Figure 2.8 shows an example of a pulse sequence.

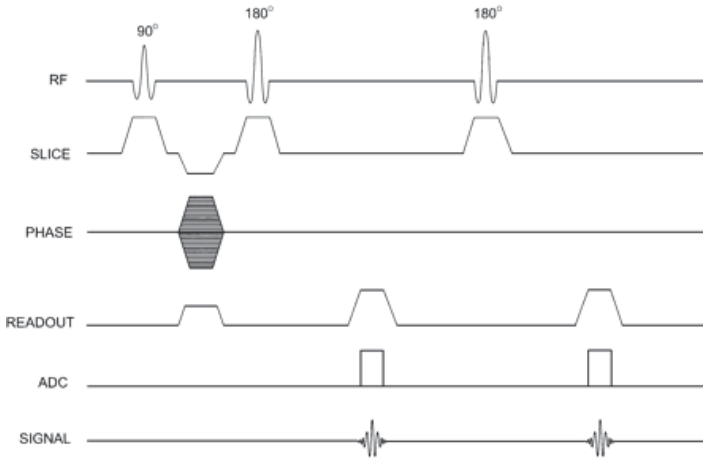


Figure 2.8: Pulse sequence diagram for raw image data collection [14].

Pulse sequences influence the MRI equivalent of the compromise between noise, resolution, and artifacts. However, patient comfort and safety, the greatest concern, adds additional complexity to acquiring high quality images.

# CHAPTER 3: PARALLEL AND SIMULTANEOUS MULTI-SLICE IMAGING

## 3.1: Parallel imaging approaches

Scan time reduction through the development of novel pulse sequences such as echo planar imaging (EPI), FLASH, and turbo spin echo (TSE) has led to new and exciting applications. However, these techniques still rely on the collection of spatial frequencies in a sequential manner. The phase-encoding step is one of the most time consuming processes during a scan, so a reduction in the number of phase-encoding steps by some factor would save considerable scan time. As a result, techniques were developed starting in the late 1980s to reduce or eliminate the phase-encoding step by collecting data in parallel using the spatial sensitivity differences of multiple receiver coils.

In 1987, a technique proposed in [15] pioneered the effort to use multiple coils during signal collection by utilizing the separately acquired data to assist the image reconstruction.

The following year a method was proposed in [16] to eliminate the phase-encoding step entirely by introducing a large number of detectors around the object. Each of the detectors would collect data depending on the proximity to each of the locations in the volume [16]. A matrix inversion reconstruction method would then be used to solve the inverse source problem, reconstructing the image. Practical issues for implementation of this method include the arrangement of the large number of coils required and the coupling issue that exists between closely spaced coils.

A somewhat similar technique to [16] was proposed in [17] requiring $N_d$ receiver coils, the same as the number of pixels in the image. In addition, they investigated some of the issues

in [16] by analyzing how decoupling of the coils can be performed, analyzing the SNR issues present when using a large number of coils, and addressing the assumptions used to develop a model of the coil sensitivities at each pixel location, which would affect the mathematics of the inverse source problem. Furthermore, a method known as combined zeugmatography and array (COZA) was proposed utilizing multiple coils, a slice-selection gradient, and an additional single readout gradient during data sampling [17]. This proposed technique could lead to a decrease in the number of coils required by a factor of $\sqrt{N_d}$ [17].

The methods in [16], [17] were not practical due to the geometrical challenges involved with setting up and using a large number of small coils in addition to managing their electromagnetic behavior.

In the early 1990s, a technique that would provide the foundations for practical spatial-domain PI was proposed in [18]. In this study, a significant reduction in the number of coils needed to collect the required data for reconstruction was made possible by sampling only a fraction $R$ of the phase-encoding lines [18]. This subencoding of $k$-space produces an aliased image where the number of pixels that need to be separated is $R$ instead of $N_d$ as in [17] and can be resolved using $N_c$ $(\geq R)$ coils [18]. Furthermore, these $R$ pixels to be separated come from locations where coil sensitivities can be sufficiently different [18]. These differences can improve the singularity problem seen in earlier methods [16], [17] that can be present in high-resolution imaging because of the large number of closely spaced coils exhibiting little sensitivity differences at each location [18].

As a practical technique to reduce scan time, PI was not experimentally successful until the late 1990s when the hardware required, SNR considerations, and methods for sensitivity assessment were thoroughly investigated. A method known as simultaneous acquisition of spatial

harmonics (SMASH) introduced in [19] would bring PI into the modern era with its ability to reduce the number of $k$-space lines encoded by approximating the missing spatial frequencies using a linear combination of weighted coil sensitivities.

Modern PI methods rely on the use of phased-array coils, pioneered in [20], to acquire the parallel data. A phased-array coil configuration is comprised of multiple small surface coils with independent data channels oriented in a particular way with respect to each other to reinforce and suppress sensitivity to various locations. While providing a larger and more uniform coverage of the image volume compared to small surface coils used individually, it can also result in an ideal SNR benefit of up to $\sqrt{N_c}$ assuming the noise in the coil elements is uncorrelated [12]. An example of a four-coil phased array and its spatial sensitivity map are shown in Figure 3.1. However, many phase-array coil configurations are not appropriate for PI applications due to the spatial sensitivity requirements [12].

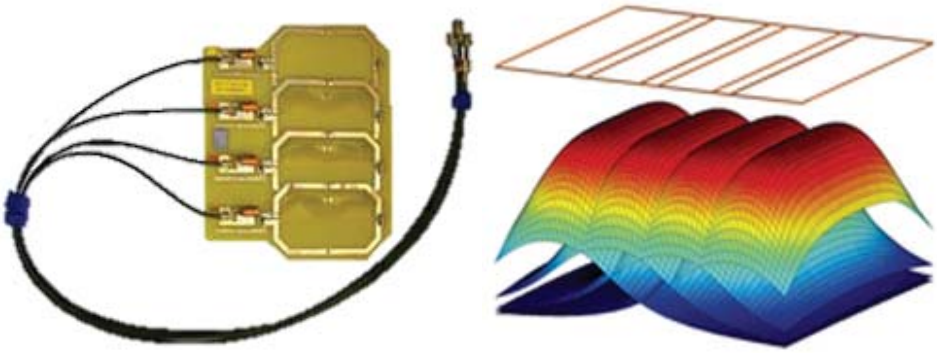

Figure 3.1: Phased-array coil with four elements (left) and its sensitivity map (right) [12].

SENSE is a spatial-domain based modern PI method developed in [2] that shares similarities to [18] where the number of sampled $k$-space lines is reduced. However, the authors expand the applicability of the method, address assumptions made about the acquisition of the

coil sensitivity reference images, and make suggestions about SNR optimization. The reduction of $k$-space lines in SENSE is performed by increasing the distance $\Delta k$ between $k$-space lines. This has the effect of reducing the field of view (FOV) by the relation

$$FOV = \frac{1}{\Delta k}. \tag{20}$$

Therefore, any signal-producing structures outside of the FOV will alias back into the reduced FOV due to the undersampled $k$-space, resulting in an image whose pixels contain superimposed signal from various locations. The extent of $k$-space undersampling is given in terms of the reduction factor $R$, representing the factor by which the number of $k$-space lines is reduced along a given direction. Figure 3.2 illustrates the FOV reduction and aliasing accompanying an acquisition with $R = 2$ along the phase-encoding direction and compares it to a normal, non-subsampled acquisition with $R = 1$. A full FOV image with no aliasing is obtained by utilizing the spatial sensitivities of a multi-coil array as an input to a linear-algebra based reconstruction method [2].

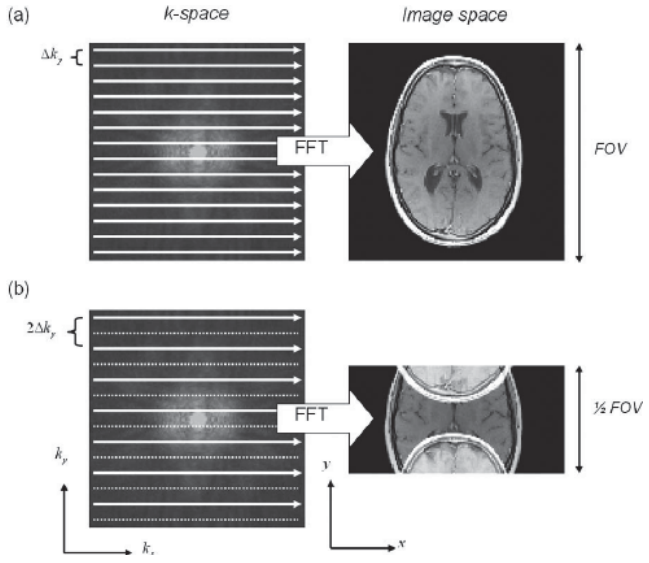


Figure 3.2: Normal (a) vs. SENSE ($R = 2$) (b) acquisition [2].

Each receiver coil that is part of an array has a specific spatial sensitivity for the imaged volume that is dependent on many factors including the particular coil configuration used. These spatial sensitivities provide a coil specific view of the raw signal and thereby each coil $\beta$ produces its own reduced FOV image $i_\beta$ of the object [2]. Therefore, a subset of the pixels in each of the individual coil images includes an intensity that is a result of aliased signal.

A model of the linear-algebra based reconstruction approach is based on describing the coil sensitivities by the matrix $C$ with elements given by [2],

$$C_{\beta,p} = c_\beta(\vec{r}_p) \tag{21}$$

where $p$ represents a superimposed pixel, $\vec{r}_p$ the position of pixel $p$, and $c_\beta$ represents the spatial sensitivity of coil $\beta$.

If noise correlation from the coils is taken into account, the inverse of the coil sensitivity matrix is given by [2]

$$U = ({C_{\beta,p}}^H \psi^{-1} C_{\beta,p})^{-1} {C_{\beta,p}}^H \psi^{-1}. \tag{22}$$

The vector $\vec{\chi}$ of pixels forming the reconstructed components of the full FOV image can be solved by [2],

$$\vec{\chi} = U\vec{I}_p \tag{23}$$

where $\vec{I}_p$ represents the vector of pixel intensities for a given pixel $p$ from each coil image $i_\beta$. Performing this operation for each pixel will reconstruct the full FOV image [2].

This reconstruction is dependent on the behavior of the coil sensitivity matrix. The inversion process is extremely sensitive to noise if the matrix to be inverted is not well conditioned. This can occur if the coil sensitivities are too similar resulting in an ill-conditioned problem with noise being amplified and folded back into the image during the reconstruction, reducing the SNR at a given pixel [2]. Therefore, coil-array arrangement, coil coupling, and

noise levels are some important factors to consider when formulating a well-conditioned system [2]. Analyzing the effect of noise due to the coil geometry is done by defining a quantity known as the geometry factor (g-factor) given by [2]

$$g_{SENSE}^{p} = \sqrt{\left[\left(C_{\beta,p}{}^{H}\psi^{-1}C_{\beta,p}\right)^{-1}\right]_{p,p}\left(C_{\beta,p}{}^{H}\psi^{-1}C_{\beta,p}\right)_{p,p}} \geq 1. \tag{24}$$

The g-factor $g_{SENSE}^{p}$, which has great influence on the SNR in a reduced $k$-space acquisition, can be included as a factor in the SNR of an accelerated protocol by [2]

$$SNR_{SENSE}^{p} = \frac{SNR_{UA}^{p}}{g_{SENSE}^{p}\sqrt{R}}. \tag{25}$$

Therefore, the target SNR for a given application can be included into the design considerations for the particular coil array employed [2].

## 3.2: Simultaneous multi-slice imaging

In conventional 2D imaging, the acquisition of raw data for slices proceeds by sampling a line of $k$-space for a particular slice sequentially. Therefore, the number of slices at a given resolution that needs to be acquired influences overall scan time. However, if a line of $k$-space for multiple slices is acquired simultaneously rather than sequentially, this can drastically reduce scan time especially in protocols that do not permit sampling lines from other slices within a given $T_R$.

A SMA can be incorporated into a protocol by applying a slice-selection RF pulse whose excitation profile includes bandwidth centered at more than one carrier frequency, thereby selecting a slice at multiple locations simultaneously.

The behavior of a SMA RF pulse with these excitation characteristics can be best understood in the frequency domain. Viewing the RF pulse in the frequency domain provides a slice profile assuming the Fourier approximation assumptions are made which are valid for flip

angles $\theta < \pi/2$ when the nonlinear behavior of the Bloch equations are not dominant [10]. The slice profile shows the range of spins the RF pulse will excite and the corresponding slice thickness in the spatial domain under a given slice-selection gradient.

To excite a slice of given characteristics at a particular location under the influence of a slice-selection gradient, shifting the bandwidth of the RF pulse to that location is required. This can be done utilizing the dual of the Fourier convolution theorem

$$\mathcal{F}[RF(t) \cdot m(t)] = \mathcal{F}[RF(t)] * \mathcal{F}[m(t)]. \tag{26}$$

If $m(t) = e^{j2\pi f_{os}t}$, then $\mathcal{F}[m(t)] = \delta(f - f_{os})$ where $f_{os}$ is the frequency offset. Substituting this result into (26) results in the shift of the spectrum of $RF(t)$ to the frequency $f_{os}$. This process, known as amplitude modulation, can be applied repeatedly using different values of $f_{os}$ to form multiple bands at different locations. When these individual modulation results are added, a composite RF pulse that can excite multiple slices simultaneously is formed.

With a SMA RF pulse, each point in the acquired $k$-space will consist of the combined data for that point from multiple slices. Therefore, many techniques have been proposed since the late 1980s to unravel the data producing the separated single-slice images.

A Hadamard-encoded SMA, developed in [21], uses RF pulses that have multi-slice excitation bands labeled with a phase. The technique requires multiple experiments to be performed, each encoding the slices with a unique phase pattern given by a Hadamard matrix transform of order $NS$ where $NS$ is the number of simultaneous slices excited [21]. The information unique to each slice is extracted from the superimposed raw data using add/subtract operations [21]. This method has many applications requiring an increase in signal; however the multiple excitations required does limit its use to reduce scan time.

A technique proposed in [22] to separate the information acquired simultaneously uses an additional gradient in the slice-selection direction applied concurrently with the readout gradient. This additional gradient adds a frequency shift to the excited slices. Assuming the receiver bandwidth is high enough, the slices will appear side by side in the final reconstructed image assuming the frequency offset is greater than the slice bandwidth [22]. A large drawback of this method is the restrictions that it places on the acquisition to avoid the blurring associated with the voxel tilting caused by the additional gradient applied along the slice-selection direction at the same time as the readout gradient.

Addressing some of the shortcomings in [21] including increased scan time and preprocessing of data during reconstruction, phase-offset multiplanar (POMP) volume imaging was introduced in [23]. A composite SMA RF pulse is used to excite several slices simultaneously. However, a $k$-space-line-dependent phase factor is given to each slice in a pattern determined by the Fourier shift theorem. This effectively moves each slice in the phase-encoding direction relative to the other slices acquired simultaneously by a distance depending on the phase cycling pattern [23]. Assuming the FOV is large enough and an appropriate shift is given to each slice in the composite pulse, the slices will not overlap in the reconstructed image [23]. However, this method requires a decrease in resolution or an increase in phase-encoding steps to provide the FOV suitable for side-by-side reconstruction of the slices.

### 3.3: SMA with parallel imaging

A more recent development introduced in [24] incorporated PI and its spatial sensitivities to reconstruct the information associated with each slice in a SMA. The pixels in each of the individual coil images now represent the superposition of signal from the same pixel in each of the slices in the SMA weighted by the slice-specific coil sensitivities at that pixel location [24].

The reconstruction of the slices is performed using matrix inversion of the coil sensitivity matrix similar to [2] but adapted for signal arising from multiple slices rather than from locations in the same plane [24]. The number of coils required to separate $NS$ slices is $N_c \geq NS$ [24]. As in related methods, to avoid an ill-conditioned coil sensitivity matrix and its associated noise amplification, slice-specific coils sensitivities need to be sufficiently different which can be a problem if the slices are close and/or if the coil array arrangement does not permit a well-posed inversion.

CAIPIRINHA introduced in [4] is a method to improve the matrix inversion reconstruction in SMA techniques that utilize PI as in [24] and employ demanding coil geometries. This technique addresses the inversion condition problem by controlling the aliasing of excited slices by employing the RF pulse phase cycling first demonstrated in [23]. If the one-dimensional spin density $\rho(y)$ is written in terms of the IDFT, it can be seen that the Fourier shift theorem given by [4],

$$\rho(y-\Delta y) = \sum_{m=-\frac{N_s}{2}}^{\frac{N_s}{2}-1} (S(m\Delta k_y)e^{-jm\Delta k_y \Delta y})e^{jm\Delta k_y y} \tag{27}$$

provides the basis for shifting the slices in a SMA by a slice-dependent distance $\Delta y$.This shows that the signal from a slice needs to be multiplied by a $k_y$-line-dependent phase factor with a cycling pattern given by [4]

$$\Phi_m = -jm\Delta k_y \Delta y. \quad m = -\frac{N}{2}, \dots, \frac{N}{2}. \tag{28}$$

Therefore, the signal from each slice excited will require a different phase pattern given by (28), providing the desired spatial shifts. In addition, the signal for a given $k$-space point will be linear

combination of the signal from each slice $l$ multiplied by their individual phase factors for that $k$-space line [4] given by

$$S(m\Delta k_y) = \sum_{l=1}^{NS} S_l(m\Delta k_y) e^{-j(m-1)(l-1)\frac{2\pi}{NS}\Delta k_y}. \quad (29)$$

These phase shifts are provided by a $k$-space-line-dependent composite SMA RF pulse whose excitation bands are phase modulated [4]. The resulting slice-dependent shifts are given by [4]

$$\Delta y(l) = (l-1)\frac{FOV}{NS}. \;\; l = 1, \dots, NS. \quad (30)$$

These shifts result in the coil sensitivities and pixel contributions to a given coil image pixel to be different. This can increase the coil sensitivity differences by taking advantage of the sensitivity differences in the phase-encoding direction [4]. The coil sensitivity matrix for a two-coil, two-slice SMA after applying a $FOV/2$ shift to one of the slices becomes [4],

$$\begin{bmatrix} i_1(x,y) \\ i_2(x,y) \end{bmatrix} = \begin{bmatrix} C_{11}(x,y) & C_{12}(x,y+FOV/2) \\ C_{21}(x,y) & C_{22}(x,y+FOV/2) \end{bmatrix} \begin{bmatrix} \rho_1(x,y) \\ \rho_2(x,y+FOV/2 \end{bmatrix} \quad (31)$$

where the spin density at each position in the slice is given by $\rho_1(x,y)$ and $\rho_2(x,y)$ for slice one and two respectively. This shows that the pixel intensities within a coil image come from the same location in slice one and from a position shifted by $FOV/2$ for slice two where the coil sensitivity could be sufficiently different to provide a better-conditioned inversion [4]. Even considering the case where the sensitivity is the same for each slice, this method can in many cases improve the condition of the sensitivity matrix enough to allow for inversion, leading to SNR improvements given by [4]

$$SNR^p_{CAIPI} = \sqrt{NS}\frac{SNR^p_{UA}}{g^p_{CAIPI}\sqrt{R}}. \quad (32)$$

Comparing this to the SENSE SNR in (25), it can be seen that SNR improvements can be made by reducing the g-factor noise associated with a coil-array configuration and the increase in

signal by $\sqrt{NS}$ provided by the additional slice data acquired during a SMA [4]. This can increase the performance of many PI applications allowing the use of higher acceleration factors [4].

These methods represent some of the diverse approaches utilizing the hardware in novel ways while appealing to unique reconstruction models. Some of these approaches would not become practical until scanner hardware and computer processing were more developed. However, because many of these advances require only modifications to software, these techniques are capable of being integrated into preexisting sequences, giving them new potential applications. In this work, the technique developed in [4] was implemented in a SDE and evaluated for a demanding coil geometry with an ill-conditioned coil sensitivity matrix. This work not only provided a demonstration of incorporating this technique into upcoming research but also confirmed the reconstruction benefits described in [4].

# CHAPTER 4: IMPLEMENTATION OF A PHASE-MODULATED SMA RF PULSE

## Introduction

Pulse sequence programming is the process of designing a particular raw data acquisition protocol for the purposes of obtaining images with certain characteristics for a given application. This process is generally performed using a particular programming language like C or C++ to instruct the MRI hardware to run various real time events such as RF pulses, gradients, and ADC sampling. Furthermore, the sequence, duration, and magnitude of these events are prescribed within the pulses sequence program to ensure the correct physical response from the spins in the imaged object, to prevent events from running that may cause damage to MRI hardware, and to safeguard the patient from any potentially harmful electromagnetic effects.

In this work, the Siemens SDE was used to implement a customized FLASH pulse sequence with a CAIPIRINHA-style RF pulse. The SDE provides a C++ framework for sequence development by providing several modular programs that support the programmer from debugging and simulation to visualization of the pulse sequence. In addition, libraries with common real-time event functionality are provided to aid in the customization of a protocol.

## 4.1: FLASH pulse sequence

FLASH is a spoiled, gradient-recalled echo (GRE) pulse sequence. The benefits that FLASH provides come from its ability to destroy the transverse magnetization after a line of $k$-space is acquired through spoiling and the use of a small flip angle. Spoiling ensures that no transverse magnetization from one $T_R$ is refocused and contributes to the signal during the next $T_R$, which could alter contrast. This spoiling process can be performed using gradient and RF

spoiling. The low flip angle combined with a reduced $T_R$, promotes a longitudinal magnetization equilibrium to form. This provides good signal at a decreased scan time. An example of a FLASH-style sequence is shown in Figure 4.1.

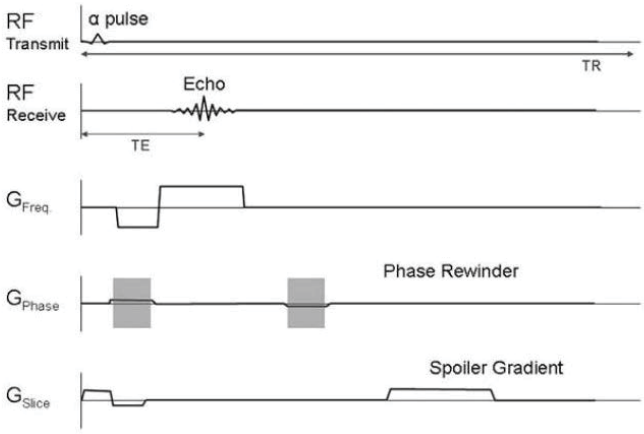


Figure 4.1: Flash-style pulse sequence diagram [25].

## 4.2: Modulation of an internal RF pulse to produce a SMA

A common RF pulse shape used as a basis for many types of excitation pulses is based on the SINC function. This has an ideal boxcar excitation profile in the frequency domain. However, due to truncation of the pulse appropriate for finite-duration applications, the excitation profile is less than ideal with ripples outside of the desired slice thickness. To improve the profile, the pulses are usually apodized with an appropriate function (commonly a Hanning or Hamming window) to improve the profile.

The base unmodulated RF pulse used in this work was an internally defined SINC pulse with a shape and slice profile like the example shown in Figure 4.2.

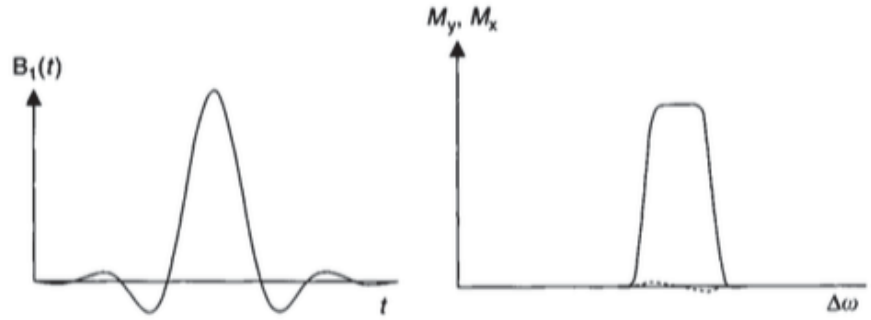


Figure 4.2: Truncated and apodized SINC pulse (left) and its slice profile (right) [10, p. 40].

The pulse has an internally defined duration and number of discrete sample points $N_s$. Using this information, the sample period was obtained by dividing the duration by $N_s$. The calculated sample period was used during the modulation step.

To perform the modulation on the basis pulse, the complex sample points were obtained by using a RF pulse class method that returned an array of structures. The complex sample points are stored in this structure with a member holding the magnitude of the complex number and a member holding the phase.

To determine what the frequency of the complex exponential modulating the RF pulse needs to be to move the bandwidth to the correct excitation location, the frequency offset relative to the isocenter needs to be calculated. This value is given by

$$f_{os} = \frac{\gamma_p}{2\pi} G_z \Delta z. \tag{33}$$

The value for $\Delta z$ will determine the distance the offset slice center will be from the isocenter while under the influence of a slice-selection gradient of strength $G_z$. These values were obtained from the user interface (UI) and from the protocol parameters. The value for $f_{os}$ was calculated for the offset slice such that the distance from its center to the center of the isocenter slice was $\Delta z = 50mm$.

The modulation of the pulse was performed according to the rules of complex exponential multiplication using a double FOR loop structure. The top loop is run according to the number of slices $NS$, that will be part of the composite pulse which in this work $NS = 2$. The top loop was designed to give each slice a multiple of $\Delta z$ modulation shift resulting in an equidistant slice-center offset relative to adjacent slices. The inner loop is performed according to the number of samples $N_s$ in the unmodulated pulse. The pulse samples that were part of the structure were converted into standard real and imaginary components for this step. This was done using the operations in the built in math libraries.

The results of this modulation was an array holding the real components at each time point of the composite pulse and another array with the corresponding imaginary components at each time point. However, the system will only accept the sample points if they are in magnitude and phase form as members of a sample structure. Using the internal math libraries, the sample points were converted to magnitude and phase and placed into an array of structures. The pulse was now ready to be input to downstream methods that would further process the pulse.

## 4.3: SMA RF phase-shift implementation

The CAIPIRINHA technique relies on imparting a distinct phase shift to each separate component of the composite pulse. The inclusion of the phase factor depends not only on the number of slices that will be excited but also on the $k$-space line. This relationship is given by (28) and (30). In this work, a shift of $FOV/2$ is considered. The result is a phase cycling at the even/odd $k$-space line of $0, \pi, 0, \pi, \ldots$ for the offset slice and $0,0,0,0, \ldots$ for the isocenter slice. The inclusion of the phase factor is a simple complex exponential multiplication that was combined with the other phase factors during the modulation step as described in section 4.2.

The result after modulation and application of the phase shifts was a set of two composite RF pulses that each excited two slices. The even line pulse gave zero shift to the isocenter and offset slice and the odd line pulse gave zero shift to the isocenter slice and a $\pi$ shift to the offset slice. In general, the number of distinct composite pulses required is determined by the phase pattern for a given shift.

### 4.4: Incorporation of the phase-modulated SMA RF pulse into a valid sequence

Before the system can run these customized pulses, various calculations are made by relevant class methods to ensure their suitability for system hardware and patient exposure. In addition, calibration steps are performed to ensure the production of the desired electromagnetic events by the various hardware components of the scanner.

#### 4.4.1: RF pulse amplitude integral and normalization

When a RF pulse in run on the system, a certain voltage is applied to the transmitter coil producing a pulse of a given duration and amplitude [26]. Initial calibrations are made by the system to determine the voltage needed to produce a rectangular pulse with a $\pi$ flip angle of a given duration [26]. This result is utilized in combination with the amplitude integral of the customized pulse to produce the desired flip angle.

The amplitude integral of the composite pulse was calculated by taking the complex modulus of each sample and adding them together [26]. This value provides a consistent way to produce a pulse with any flip angle and duration by linearly scaling the transmitter voltage with a given pulse shape. This is done by comparing the amplitude integral of the customized pulse shape with the amplitude integral calculated during the transmitter calibration step above.

The system will only accept the RF pulse samples if they normalized [26]. This format gives a standardized way of representing the pulse shapes internally for further processing. The

modulus of each sample was divided by the maximum modulus in the pulse to produce the normalized RF samples.

However, for customized pulses, the normalized pulses samples will produce a lower than expected flip angle [27]. In order to ensure that the system will produce the correct flip angle, a modified amplitude integral needs to be provided to the appropriate pulse preparation class method [27]. The amplitude integral that needs to be provided was calculated by computing the amplitude integral of the unmodulated internal RF pulse and dividing it by the maximum modulus value present in the final modulated composite pulse [27]. The pulse(s) are then prepared by class methods that calculate energy and run checks [26]. After preparation, the pulses are ready to become part of the sequence that instructs the MRI hardware to run the pulse events in real time.

#### 4.4.2: Incorporation of the RF pulse into a real-time event

The framework for running the real-time objects is a series of libraries that interact closely with the microcontrollers that handle the various components of system. The methods associated with linking the real-time events into a coherent and well-timed sequence of events require several inputs, including a variable that indicates when the objects should start and pointers to prepared events like gradients, ADCs, and RF pulses.

The acquisition of the $k$-space lines require looping over the real-time events in a particular way depending on the sequence. For this customized FLASH sequence with the customized CAIPIRINHA pulse, the phase pattern dictated by the $FOV/2$ shift required that there were two composite pulses that were each ran depending on whether the $k$-space line being acquired was even or odd. To specify the correct composite RF pulse to use at each loop cycle, a conditional was employed to test whether the current line being acquired was even or odd. The

appropriate pointer to the even or odd composite pulse will then be used as an input to the method that will run that pulse on the system hardware. This continued until all the $k$-space lines were acquired.

## 4.5: Slice position calibration

The customized FLASH sequence along with the amplitude and phase-modulated RF pulse was used to acquire several sets of images to confirm the slice locations excited and the phase shift given to the offset slice.

A Siemens water phantom was used to confirm the excitation of the correct slices by marking the phantom with vitamin E pills at the target slice locations A and B as shown in Figure 4.3. The phantom was positioned in the scanner using the laser target such that the isocenter was defined to be at slice B.

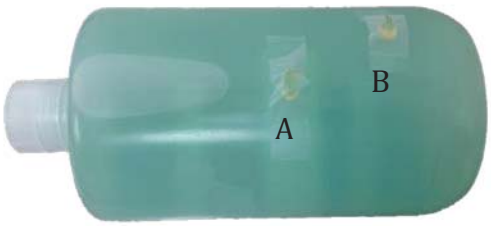


Figure 4.3: Water phantom with slice locations marked with vitamin E pills.

A 3T TRIO scanner (Siemens Medical Solutions, Erlangen, Germany) with a 32-channel head coil was used to acquire the calibration images using a conventional FLASH sequence without SMA to provide a reference for the image quality of the two transverse slices to be excited simultaneously. The acquisition parameters used are as follows: FOV = 250 mm X 250 mm, matrix size = 256 X 256, $\theta = 15^{\circ}$, slice thickness = 10 mm, $T_R = 12$ ms, $T_E = 6$ ms.

These images are shown in Figure 4.4 with target locations indicated by the vitamin E pill distortions at the top of the phantom. These images were both windowed to show that the distortion at the top of each image in Figure 4.4 is consistent with the location of the vitamin E pills as shown in Figure 4.5.

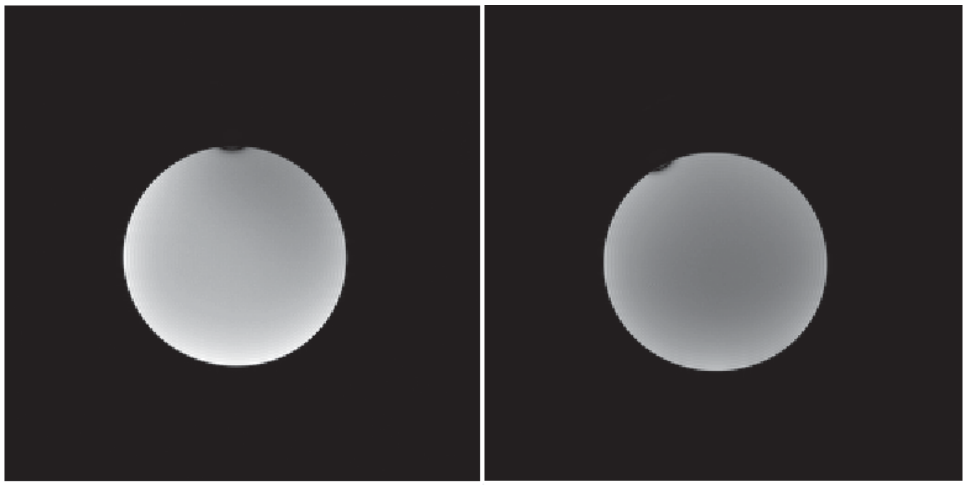

Figure 4.4: Single-slice reference excitations of slice A (left) and B (right).

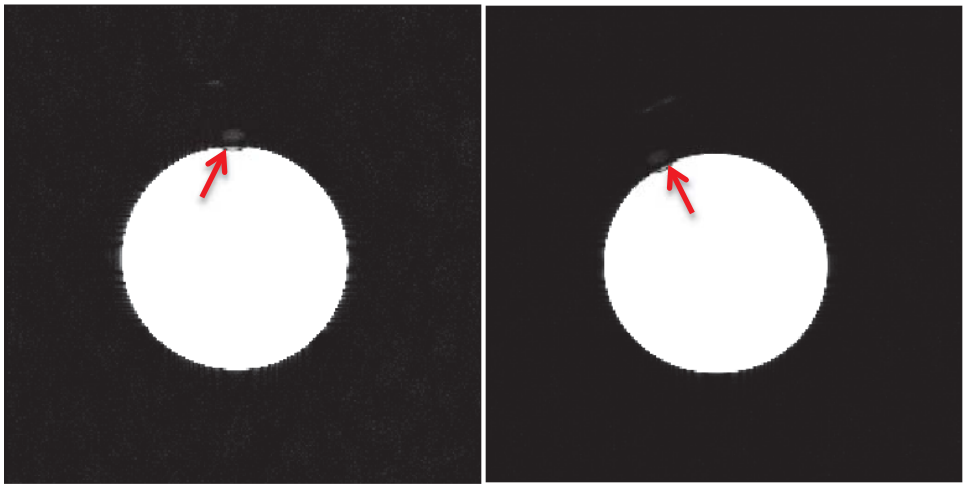

Figure 4.5: Windowed versions of slice A (left) and B (right) indicating vitamin E pill locations (red arrows).

## 4.6: Results for a two-slice CAIPIRINHA pulse

This experiment was performed using the two-slice CAIPIRINHA FLASH sequence that was developed in this work along with the scanner and phantom used in section 4.5. For the first acquisition, the FOV was greater than twice the object size in both the phase and frequency-encoding directions. The imaging parameters used for this acquisition were the following: FOV = 250 mm X 250 mm, matrix size = 256 X 256, $\theta = 15^{\circ}$, slice thickness = 10 mm, $T_R = 12$ ms, $T_E = 6$ ms. The second acquisition illustrates the aliasing that occurs when the FOV in the phase-encoding direction is reduced to less than the dimensions of the object which can occur when using SENSE with a large acceleration factor. The imaging parameters used for this scenario were the following: FOV = 150 mm X 150 mm, matrix size = 256 X 256, $\theta = 15^{\circ}$, slice thickness = 10 mm, $T_R = 12$ ms, $T_E = 6$ ms. Figure 4.6 shows the acquired images for the aliased and non-aliased acquisitions.

These results show that the development and implementation of a CAIPIRINHA composite RF pulse that simultaneously excited two slices at predefined locations and applied a spatial shift of $FOV/2$ to the offset slice was successful.

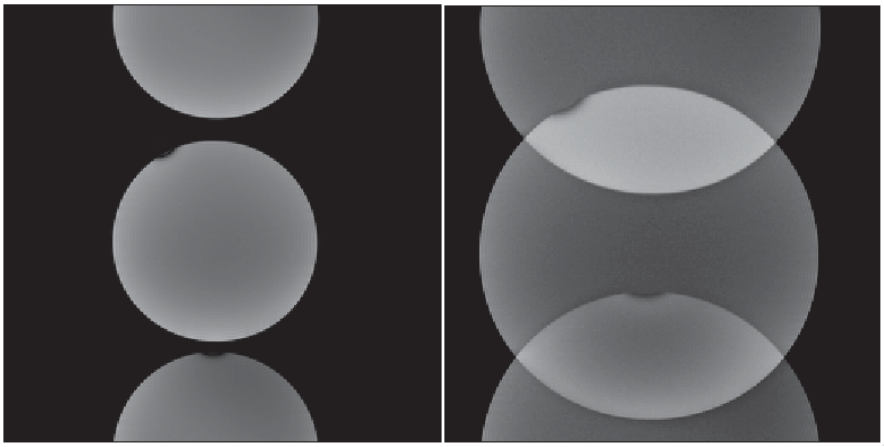

Figure 4.6: POMP-style acquisition with $FOV \geq 2FOV_{object}$ and slice shift $FOV/2$ (left) and SENSE combined with a POMP-style acquisition exhibiting aliasing with $FOV < 2FOV_{object}$ and a slice shift of $FOV/2$ for the off-center slice (right).

## CHAPTER 5: SIMULATION OF A CAIPIRINHA SLICE RECONSTRUCTION

### Introduction

The goal of implementing the RF pulse in this work was to form the foundation for customizing fast protocols that implement CAIPRINIHA acquisition schemes. To demonstrate the benefits of using a CAIPRININA acquisition, a simulated reconstruction of a two-slice SMA was performed under extreme inversion conditions imposed by a difficult coil geometry utilizing only two coils. Two scenarios were considered: A non-CAIPIRINHA with SENSE ($R = 2$) acquisition with added noise and a CAIPIRINHA with SENSE ($R = 2$) acquisition with added noise.

The sum-of-squares (SOS) images used in the simulated reconstruction were acquired with an American Academy of Radiology (ACR) phantom on a Siemens 3T TRIO scanner with 2-element spine coil and 2-element body coil using the SMA FLASH sequence developed in Chapter 4. The following parameters were used during the acquisition of these images: FOV = 220 mm X 220 mm, matrix size = 256 X 256, $\theta = 15^{\circ}$, slice thickness = 2 mm, $T_R = 12$ ms, $T_E = 6$ ms, 10 signal averages. The slice positions were taken at isocenter and at a location off center by 100 mm. The coil sensitivity maps were simulated using smoothly varying values for the weights at each pixel. Reconstruction of the images was performed using an in-house developed script in Matlab (The MathWorks, Inc., Natick, MA, United States).

### 5.1: Simulation of coil sensitivity images

To demonstrate an extreme case where CAIPRINHA will have SNR and unfolding benefits, the coil sensitivity at each pixel was simulated to provide the slices with no distinction

in the slice-selection direction. In addition, the two slices will exhibit the same phase-encoding direction sensitivities. This will provide the reconstruction algorithm an example of a worst case scenario for inversion of the coil sensitivity matrix, the resulting noise amplification and unfolding of the aliased pixels. Coil one sensitivity maps were obtained by giving each row in the matrix a number between zero and one by evaluating an exponentially decaying function of the pixel position. Coil two sensitivity maps were created by subtracting the values obtained for coil one at each pixel from one. The results for each coil were masked to provide only coil sensitivity to locations in the imaged object by thresholding the SOS images shown in Figure 5.3 and creating a binary mask which was then applied to the coil sensitivity images. Extrapolation and polynomial fitting of the maps were not considered for the simulation conditions. The resulting sensitivity maps for coil one and two for both slices are shown in Figure 5.1 and Figure 5.2 respectively.

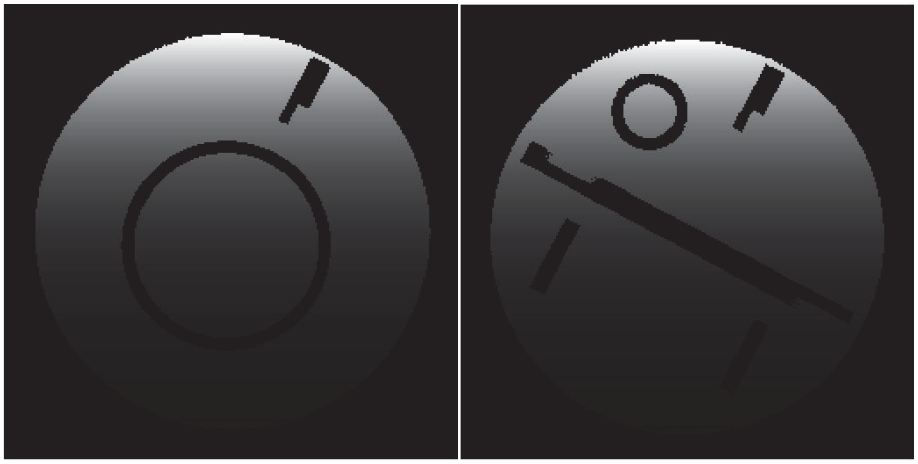

Figure 5.1: Sensitivity maps for coil one. Slice one (left) and slice two (right).

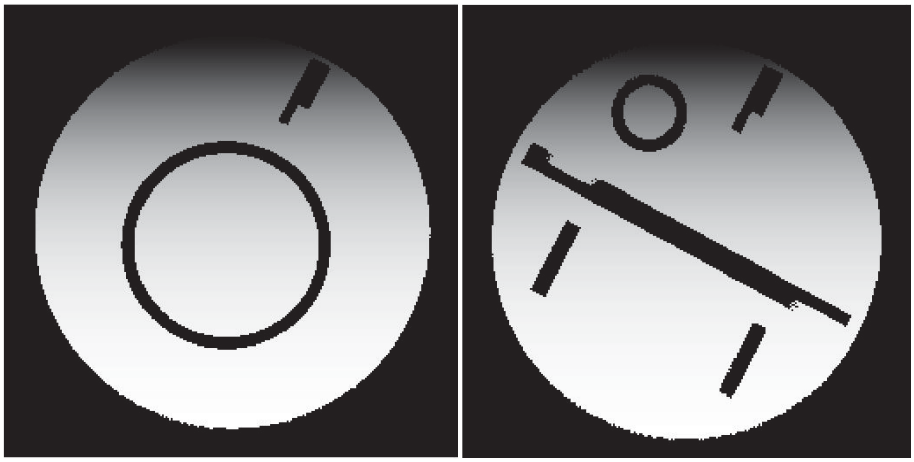

Figure 5.2: Sensitivity maps for coil two. Slice one (left) and slice two (right).

## 5.2: Simulation of coil images

The coil images for each coil were produced by taking the SOS images for both slices shown in Figure 5.3 and weighting them according to the coil sensitivities in Figure 5.1 and Figure 5.2. The weighted slice images were added together to simulate a simultaneous two-slice acquisition and white Gaussian noise of equal mean and variance was added to both sets of images, producing the coil images shown in Figure 5.4 and Figure 5.5 simulating a non-CAIPIRINHA with SENSE ($R = 2$) acquisition with noise and a CAIPRINIHA with SENSE ($R = 2$) acquisition with a $FOV/2$ shift and noise respectively.

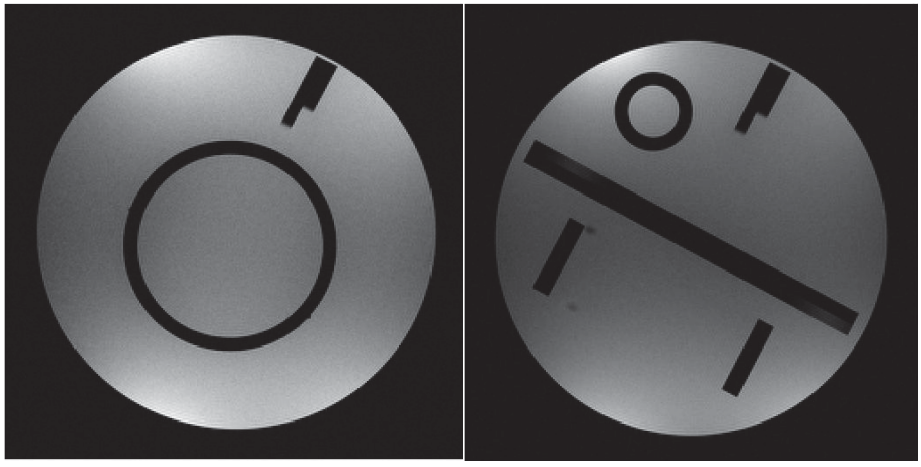

Figure 5.3: SOS images for slice one (left) and slice two (right).

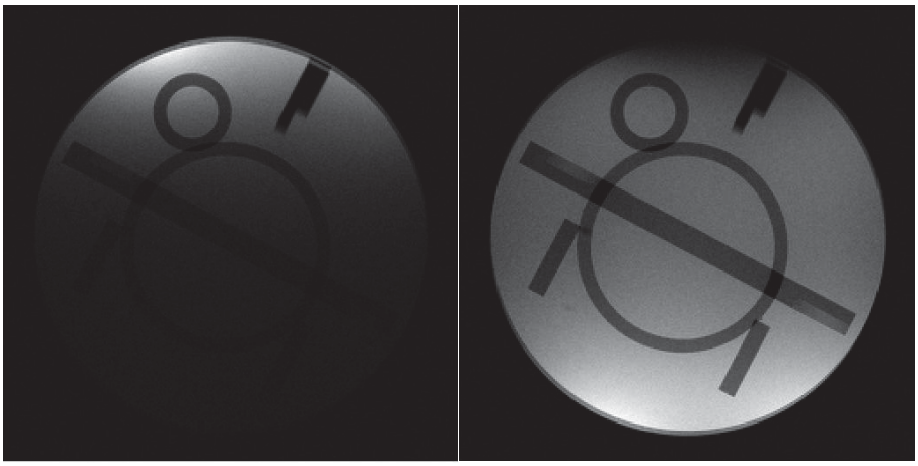

Figure 5.4: Non-CAIPIRINHA with SENSE ($R = 2$) images with added noise for coil one (left) and coil two (right).

Figure 5.5: CAIPIRINHA with SENSE ($R = 2$) images with added noise for coil one (left) and coil two (right).

## 5.3: Results of a simulated CAIPIRINHA reconstruction

The CAIPIRINHA reconstruction model in (31) was adapted and implemented in a custom Matlab script given in the Appendix to reconstruct slices one and two for the scenarios considered.

In scenario one, a SENSE ($R = 2$) acquisition of two slices without a CAIPIRINHA phase shift applied, simulated in Figure 5.4, was used to demonstrate the ineffective reconstruction that results from the coil sensitivity matrix being highly ill-conditioned. This

resulted from the lack of sensitivity difference in the slice-selection and phase-encoding directions. The result of this reconstruction for slices one and two is shown in Figure 5.6. The inversion process resulted in highly noisy and incomplete unfolding of the images. Both slices appear to be similar in appearance with information from both slices still present.

In the second scenario, a SENSE ($R = 2$) acquisition now with the CAIPIRINHA phase shift of $FOV/2$ given to the offset slice, simulated in Figure 5.5, demonstrated the effectiveness of this technique in the extreme inversion conditions imposed by the simulated coil-array geometry and slice positioning. The results of this reconstruction are shown in Figure 5.7.

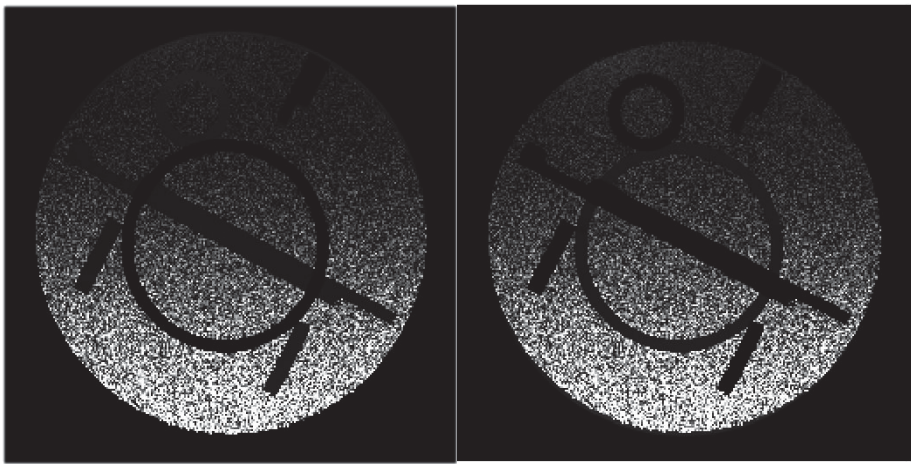

Figure 5.6: Reconstruction of slice one (left) and slice two (right) for a non-CAIPIRINHA with SENSE ($R = 2$) acquisition.

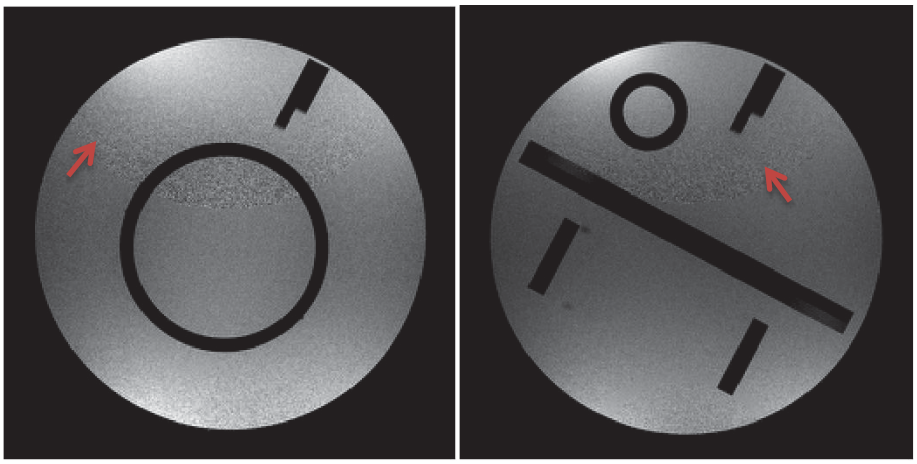

Figure 5.7: Reconstruction of slice one (left) and slice two (right) for a CAIPIRINHA with SENSE ($R = 2$) acquisition showing areas of noise amplification (red arrows).

The reconstructed slices in this scenario show that by shifting the offset slice, the phase-encoding sensitivity differences within a given slice could be exploited. This resulted in a coil sensitivity matrix that was better conditioned, giving significantly improved results. The unfolding of both slices was much more complete, preserving the contrast existing in the original SOS images in Figure 5.3. The general noise level is largely decreased, only showing the expected locally increased noise in positions of aliasing and associated extra demand placed on the inversion. This local noise amplification is demonstrated in Figure 5.7 by the red arrows.

The benefits of the CAIPIRINHA technique exhibit the expected SNR and unfolding benefits in the worst-case scenario chosen for this simulation. Applications which permit greater coil array flexibility and more relaxed protocol parameters can get better SNR and unfolding effects than demonstrated here with increased slice-selection and phase-encoding direction sensitivity differences between slices. In addition, as the authors of [4] suggest, this technique may be used to increase the acceleration factor of many PI methods, further decreasing scan time while limiting some of the accompanying increase in noise and artifacts.

# CHAPTER 6: FUTURE WORK AND CONCLUSION

## Introduction

The methods described and implemented in this work allow for the addition of these techniques to already existing sequences. This will allow the extension of those protocols and provide unique routes to approach experimental problems. In addition, the ability to efficiently customize and create new parameters for a sequence within the software environment will add additional flexibility.

## 6.1: Implementation of CAIPIRINHA in a single-shot EPI sequence

In addition to novel acquisition and reconstruction methods to decrease scan time, many unique pulse sequences have been developed to accomplish this goal. EPI is a pulse sequence that allows for the acquisition of many lines of $k$-space for a slice within one excitation. An EPI sequence can be single-shot where all the lines of $k$-space for a slice are acquired after one excitation or multi-shot where a subset of the $k$-space lines are acquired after one excitation. An example of a GRE single-shot EPI sequence is shown in Figure 6.1.

To add additional flexibility to an EPI sequence, CAIPRINHA can be utilized to add an additional component of acceleration to the protocol. CAIPRINHA requires that phase shifts be supplied to each slice with a particular $k$-space-line-dependent pattern [4]. These phase shifts are delivered by phase-modulating the composite RF pulse component associated with a particular slice during slice selection [4]. However, the structure of an EPI sequence may include only one RF excitation. Therefore, the typical RF phase modulations cannot be realized.

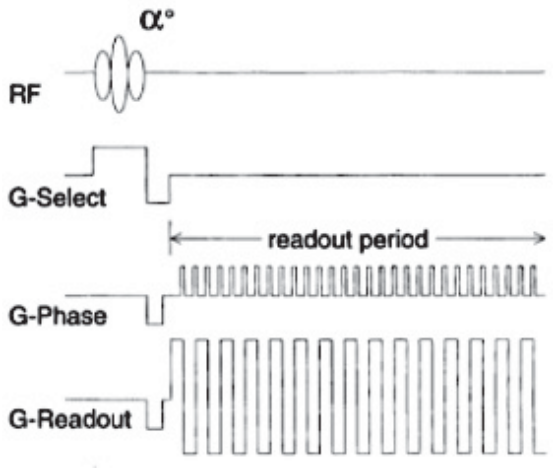


Figure 6.1: GRE single-shot EPI pulse sequence [28].

A method called blipped-CAIPI developed in [29], adapts the CAIPIRINHA method for use in EPI. Instead of phase modulating the RF pulse used to acquire a given *k*-space line, blipped-CAIPI takes advantage of the blipped nature of the phase-encoding gradients used to move the acquisition through *k*-space line by line. This is done by incorporating an additional *k*-space-line-dependent blipped gradient in the slice-selection direction to impart the desired phase to each slice in a SMA according to the phase pattern required [29]. This will provide the spatial shift associated with a CAIPIRINHA acquisition.

This method will be adopted to implement CAIPIRINHA into a customized EPI sequence that will have applications in future dynamic studies requiring significant acceleration.

## 6.2: Customization of the UI for sequence parameter selection

The sequence events in this work can be customized to give additional flexibility to the user by allowing the specification of various parameters utilized during the modulation of the RF pulse and the application of the CAIPIRINHA slice phase shift.

The Siemens environment provides a UI that allows various parameters of a particular sequence to be specified. There are various libraries that are a part of the SDE that handle the

usage of the inputs from the UI in the protocol. To add flexibility, there is a framework for allowing the sequence developer to include multiple customized parameters into the standard UI for a protocol. The section of the UI that is customizable is called the sequence special card. The behavior of the special card UI is handled by internal classes that can be structured to give the desired behavior.

A library exists that enables the efficient inclusion of special card elements into the UI. This library includes various classes and methods that allow the customization of element positions, data type, input styles (drop down selection, check box, numerical input, etc.), units, and tool tips.

This library will be used to incorporate several useful parameters involved in a SMA with CAIPIRINHA protocol. The ability to select the number of slices that will be part of the simultaneous excitation to the right and to the left of the isocenter will be included. Furthermore, the ability to select the CAIPIRINHA shift as a fraction of the FOV will be added, allowing for the automatic calculation of the proper phase pattern to be given to the slices during the modulation steps.

## Conclusion

The successful development and implementation of a CAIPIRINHA SMA RF pulse in the Siemens SDE demonstrates that these methods can be easily customized within software to provide the desired acceleration effect for novel research applications. Furthermore, the simulation of the benefits of using this pulse in a CAIPRINHA with SENSE acquisition was shown. In particular, the simulated demanding coil geometry imposed on the matrix inversion show that significant SNR and image unfolding benefits can be achieved in applications that require less than desired coil-array flexibility.

Increased scan-time acceleration enabled by these techniques is of upmost importance for patient comfort and increased efficiency in the clinical setting. In addition, the ability to add this protocol flexibility to advanced applications will continue to be a boon for future research.

# APPENDIX: CAIPIRINHA SLICE RECONSTRUCTION ALGORITHM

```
%{
This performs a CAIPIRINHA style reconstruction of two slices excited
simultaneously acquired with two coils and a shift of the offset slice
by FOV/2.
%}

%{
The coil sensitivity images for each coil at each slice location and the
coil images with the superimposed slices needs to
be loaded into the workspace.
%}

%{
Matrix of sensitivity weightings

 csens_1_1.....csens_1_2

 csens_2_1.....csens_4_2

%}

%coil sensitivity maps, csens_coil#_slice#
%coil images for two-coil acquisition, coil_1_ima, coil_2_ima

%Inputs: The dimension of the images, "dimx" and "dimy".

dimx=input('Enter the dimension in the x direction ');
dimy=input('Enter the dimension in the y direction ');

%In this scenario, the coil images, sensitivity maps and final
%separated images have the same dimensions dimx and dimy.

%Outputs: Two image matrices representing the separated slices: slice_1 %and
slice_2.

%Declaration of the two matrices with dimensions dimx and dimy that will
%hold the final separated slice information.

slice_1=zeros(dimy,dimx);
slice_2=zeros(dimy,dimx);

%Holds the reconstructed pixel values for slice_1(j,k) and slice_2(j,k)
slicespix=zeros(2,1);

%{
To reconstruct the pixels(j,k)for each individual slice,the pseudoinverse of
the coil sensitivity matrix in found. This result is multiplied by the
column vector of the coil image pixels(j,k). The result is a 2x1 vector
where (1,1) belongs to slice_1(j,k) and (2,1) belongs to slice_2(j,k). This
is performed for all pixels dimy x dimx.
%}
```

```
for j=1:dimy
    for k=1:dimx

      %Two coil reconstruction
            slicespix=pinv([csens_1_1(j,k),csens_1_2(j,k);csens_2_1(j,k),...
                csens_2_2(j,k)])*([coil_1_ima(j,k);coil_2_ima(j,k)]);

      slice_1(j,k)=slicespix(1,1);
      slice_2(j,k)=slicespix(2,1);

    end
end

%Shift the position of the pixels in the slice 2 image matrix by dimy/2
%due to the reconstructed pixel intensity at (j,k) coming from the
%position(j+dimy/2,k).This was a result of the CAIPIRINHA shift.

slice_2=circshift(slice_2,dimy/2);
```

# REFERENCES


[1] M. A. Griswold *et al.*, "Generalized autocalibrating partially parallel acquisitions (GRAPPA)," *Magnetic Resonance in Medicine*, vol. 47, no. 6, pp. 1202–1210, Jun. 2002.

[2] K. P. Pruessmann, M. Weiger, M. B. Scheidegger, and P. Boesiger, "SENSE: Sensitivity encoding for fast MRI," *Magnetic Resonance in Medicine*, vol. 42, no. 5, pp. 952–962, Nov. 1999.

[3] D. J. Larkman, J. V. Hajnal, A. H. Herlihy, G. A. Coutts, I. R. Young, and G. Ehnholm, "Use of multicoil arrays for separation of signal from multiple slices simultaneously excited," *Journal of Magnetic Resonance Imaging*, vol. 13, no. 2, pp. 313–317, Feb. 2001.

[4] F. A. Breuer, M. Blaimer, R. M. Heidemann, M. F. Mueller, M. A. Griswold, and P. M. Jakob, "Controlled aliasing in parallel imaging results in higher acceleration (CAIPIRINHA) for multi-slice imaging," *Magnetic Resonance in Medicine*, vol. 53, no. 3, pp. 684–691, 2005.

[5] M. N. J. Paley, K. J. Lee, J. M. Wild, P. D. Griffiths, and E. H. Whitby, "Simultaneous parallel inclined readout image technique," *Magnetic Resonance Imaging*, vol. 24, no. 5, pp. 557–562, Jun. 2006.

[6] Maschen, "Spin half angular momentum," 2011. [Online]. Available: https://en.wikipedia.org/wiki/Spin-%C2%BD#/media/File:Spin_half_angular_momentum.svg. Accessed: May 10, 2016.

[7] Mi. Puddephat, "The principles of magnetic resonance imaging," in *VoxelCube*, 2016. [Online]. Available: http://www.voxelcube.com/articles/1/the-principles-of-magnetic-resonance-imaging. Accessed: May 10, 2016.

[8] A. De Silva, V. Salem, P. M. Matthews, and W. S. Dhillo, "The Use of Functional MRI to Study Appetite Control in the CNS," *Experimental Diabetes Research*, vol. 2012, no. Article ID 764017, pp. 1–13, May 2012. [Online]. Available: http://dx.doi.org/10.1155/2012/764017. Accessed: May 10, 2016.

[9] J. W. Cooley and J. W. Tukey, "An algorithm for the machine calculation of complex Fourier series," *Mathematics of Computation*, vol. 19, no. 90, pp. 297–301, Apr. 1965.

[10] M. A. Bernstein, K. F. King, and X. J. Zhou, *Handbook of MRI pulse sequences*. United States: Elsevier Science, 2004.

[11] D. M. Higgins, "ReviseMRI.com: Slice selection," 2003. [Online]. Available: http://www.revisemri.com/questions/creating_an_image/slice_selection. Accessed: May 12, 2016.

[12] A. D. Elster, "Real v Imaginary Signals," in *Questions and Answers in MRI*, 2015. [Online]. Available: http://mriquestions.com/real-v-imaginary.html. Accessed: May 12, 2016.

[13] C. B. Paschal and H. D. Morris, "K-space in the clinic," *Journal of Magnetic Resonance Imaging*, vol. 19, no. 2, pp. 145–159, 2004.

[14] "MRI pulse sequence: Multiecho spin echo MRI pulse sequence," 2014. [Online]. Available: http://mri-pulse.blogspot.com/2013/07/multiecho-spin-echo-mri-pulse-sequence.html. Accessed: May 14, 2016.

[15] J. W. Carlson, "An algorithm for NMR imaging reconstruction based on multiple RF receiver coils,"*Journal of Magnetic Resonance*, vol. 74, no. 2, pp. 376–380, Sep. 1987.

[16] M. Hutchinson and U. Raff, "Fast MRI data acquisition using multiple detectors," *Magnetic Resonance in Medicine*, vol. 6, no. 1, pp. 87–91, Jan. 1988.

[17] D. Kwiat, S. Einav, and G. Navon, "A decoupled coil detector array for fast image acquisition in magnetic resonance imaging," *Medical Physics*, vol. 18, no. 2, pp. 251–265, Mar. 1991.

[18] J. B. Ra and C. Y. Rim, "Fast imaging using subencoding data sets from multiple detectors," *Magnetic Resonance in Medicine*, vol. 30, no. 1, pp. 142–145, Jul. 1993.

[19] D. K. Sodickson and W. J. Manning, "Simultaneous acquisition of spatial harmonics (SMASH): Fast imaging with radiofrequency coil arrays," *Magnetic Resonance in Medicine*, vol. 38, no. 4, pp. 591–603, Oct. 1997.

[20] J. S. Hyde, A. Jesmanowicz, W. Froncisz, J. Bruce Kneeland, T. M. Grist, and N. F. Campagna, "Parallel image acquisition from noninteracting local coils," *Journal of Magnetic Resonance (1969)*, vol. 70, no. 3, pp. 512–517, Dec. 1986.

[21] S. P. Souza, J. Szumowski, C. L. Dumoulin, D. P. Plewes, and G. Glover, "SIMA: Simultaneous multislice acquisition of MR images by Hadamard-encoded excitation," *Journal of Computer Assisted Tomography*, vol. 12, no. 6, pp. 1026–1030, Nov. 1988.

[22] J. B. Weaver, "Simultaneous multislice acquisition of MR images," *Magnetic Resonance in Medicine*, vol. 8, no. 3, pp. 275–284, Nov. 1988.

[23] G. H. Glover, "Phase-offset multiplanar (POMP) volume imaging: A new technique," *Journal of Magnetic Resonance Imaging*, vol. 1, no. 4, pp. 457–461, Jul. 1991.

[24] D. J. Larkman, J. V. Hajnal, A. H. Herlihy, G. A. Coutts, I. R. Young, and G. Ehnholm, "Use of multicoil arrays for separation of signal from multiple slices simultaneously excited," *Journal of Magnetic Resonance Imaging*, vol. 13, no. 2, pp. 313–317, Feb. 2001.

[25] E. Lin, "Body MRI Sequences: A Conceptual Framework," in *Medscape*, 2012. [Online]. Available: http://www.medscape.com/viewarticle/759443_3. Accessed: Jun. 14, 2016.

[26] *IDEA Manual*, Siemens Medical Solutions, Erlangen, DE, 2009.

[27] D. Purdy, "Computation of RF Amplitude Integral (v1.2)," 2004. [Online]. Available: IDEA Discussion Boards. Accessed: Nov. 2015.

[28] M. K. Stehling, F. Schmitt, and R. Turner, *Echo-planar imaging: Theory, technique and application*. Germany: Springer-Verlag Berlin and Heidelberg, 1998.

[29] K. Setsompop, B. A. Gagoski, J. R. Polimeni, T. Witzel, V. J. Wedeen, and L. L. Wald, "Blipped-controlled aliasing in parallel imaging for simultaneous multislice echo planar imaging with reduced g-factor penalty," *Magnetic Resonance in Medicine*, vol. 67, no. 5, pp. 1210–1224, May 2012.